ACS OMEGA

Open Access

http://pubs.acs.org/journal/acsodf

Article

Investigation into the Performance and Mechanism of BiOX Photocatalytic Degradation of Toluene under Sunlight

Zhenlian Fan, Shirui Zhang, Shuyan Cheng, Zhengjun Feng, Hongzhou Lv, and Huiping Song*

Cite This: *ACS Omega* 2025, 10, 15082−15095

Read Online

ACCESS | Metrics & More | Article Recommendations | Supporting Information

ABSTRACT: The existence of indoor volatile organic compound pollution cannot be ignored. The main representative pollutant, toluene, poses a serious danger to human health. In this study, BiOX (X = Cl, Br, I) nanophotocatalytic materials were synthesized using a straightforward chemical precipitation process. The materials' fundamental structure and characteristics were examined, and it was investigated whether they can remove toluene gas pollutants when put them under sunlight. According to the results, within 120 min, the degradation rates of toluene are ranked as BiOCl > BiOI > BiOBr, with BiOBr achieving 16.16%, BiOI 28.13%, and BiOCl exhibiting the highest degradation efficiency at approximately 56.41%. Toluene was entirely broken down with fewer intermediates, according to the conversion rate of CO_2, the degradation product. There was also extensive research on the photocatalytic mechanism of BiOCl under sunlight. The π-bonds within the toluene benzene ring were broken by the active radicals •OH and $\bullet O_2^-$. Furthermore, the oxygen vacancies and the holes (h^+) worked in concert to enhance the toluene molecule's adsorption and activation, which accelerated the breakdown of toluene into short-chain molecules, and it became carbon dioxide and water, eventually. These reactions were considered to be environmentally and friendly. The study gives a practical way to lessen indoor VOC pollution and theoretical evidence for BiOCl photocatalytic degradation of toluene gas.

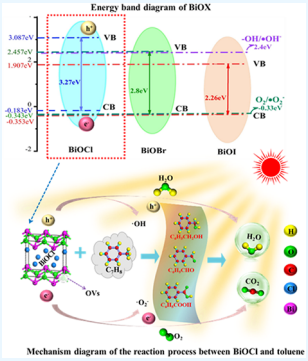

1. INTRODUCTION

With the improvement of indoor environments and the advancement of decoration technologies, the emission of a large number of organic compounds has led to increasingly prominent issues of indoor air pollution. Volatile organic compounds (VOCs) are organic compounds with high saturated vapor pressure (greater than 13.33 Pa), low boiling point, small molecular weight and easy to volatilize at room temperature under standard conditions, commonly used as VOC or VOCs, and common VOCs are benzene, toluene, xylene, styrene and trichloroethylene, trichloromethane, etc.[1−4] The release of these compounds into indoor air can engender indoor VOCs pollution.[5−7] Indoor VOCs pollution has been associated with headaches, eye irritation, and allergic reactions. Prolonged exposure may increase the risk of cancer and adversely affect reproductive and nervous system health.[5,8] Toluene, a prototypical indoor VOC, exhibits high toxicity, and chronic exposure can lead to neurasthenia and liver damage. In severe cases, it may induce leukemia, posing a particularly significant threat to the health of children and pregnant women.[9−11] Therefore, the reduction of toluene gas emissions and the control of indoor air pollution are important measures for the protection of the environment and health. It is urgent and important to explore efficient and sustainable VOCs degradation technology.[12] Technologies for the degradation of VOCs encompass absorption and adsorption, biodegradation, thermal catalytic oxidation, and photocatalytic oxidation (PCO).[13] Photocatalytic technology distinguishes itself among these methodologies, largely due to its efficiency and cost-effectiveness in environmental purification. Under illuminated conditions, photocatalytic technology facilitates the generation of electron−hole pairs via photocatalysts such as TiO_2, subsequently inducing redox reactions that decompose VOCs into innocuous molecules, including carbon dioxide and water.[14] Furthermore, photocatalytic technology boasts mild operating conditions, rapid reaction kinetics, and the capability to completely mineralize a broad spectrum of organic compounds without causing secondary pollution, highlighting its significant potential in the realm of air purification. Therefore, the photocatalytic degradation of toluene gas holds great promise.[15,16]

Photocatalytic degradation utilizes light to energize electrons on the catalyst's surface, generating electron−hole pairs. These reactive electrons and holes can then interact with toluene, breaking them down into harmless substances. This process is highly efficient and safe, making it well-suited for indoor toluene degradation.[17,18] There are various types of photocatalytic materials. In recent years, bismuth-based materials have garnered significant attention from researchers as a new type of photocatalyst, following titanium dioxide and graphitic

Received: November 24, 2024
Revised: February 4, 2025
Accepted: April 3, 2025
Published: April 9, 2025

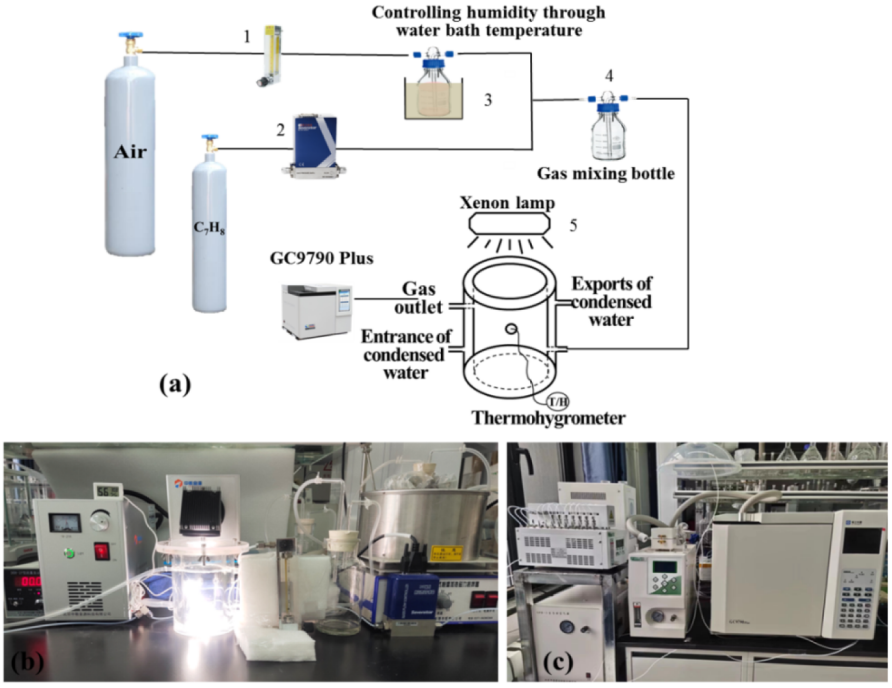

Figure 1. Schematic and physical diagram of the experimental setup: (a) Schematic diagram of the device for photocatalytic degradation of toluene; (b) physical drawing of the device; (c) device for toluene gas detection. (Note: all figures were taken by first author Z.L. Fan).

carbon nitride. Bismuth-based photocatalytic material is a new type of environmentally friendly material with good photocatalytic performance and chemical stability, which has great potential in degrading toluene gas organic compounds.[19]

In the research of bismuth-based photocatalytic materials, bismuth-based semiconductor materials such as BiOX,[20] Bi_2O_3,[21] Bi_2WO_6,[22] $BiVO_4$,[23] $Bi_2O_2CO_3$[24] and so on were widely used. These materials have a narrow energy gap and high photocatalytic activity and can effectively absorb visible and ultraviolet light, thereby achieving efficient degradation of VOCs. BiOX (X = Cl, Br, I) is a common type of bismuth-based photocatalytic material, which has the advantages of high photocatalytic activity, chemical stability, corrosion resistance and nontoxic properties, making it suitable for a wide range of applications.[25] BiOX belongs to the crystal structure of a symmetrical tetragonal system and features a unique layered structure with an indirect band gap. The layers are connected through weak van der Waals forces, creating ample space between the layers and the X atomic layer. This arrangement is conducive to the polarization of related atoms and orbitals, leading to the generation of an internal electric field between the layers and the hole, which can promote the separation of photogenerated electron and hole pairs, thus showing different photogenerated electron and hole separation efficiency through the variation of different X elements.[26−29] BiOX generally shows good catalytic activity in many photocatalytic reactions and has great potential in the photocatalytic degradation of VOCs. Currently, BiOX can be used to degrade NO_x[30] and CO_2 reduction.[31] BiOX has made significant progress in the degradation of VOCs. BiOX can be supported on geopolymer microspheres for the degradation of formaldehyde gas, with BiOI demonstrating the highest performance, achieving a degradation rate of 87.46%.[32] BiOCl supported on mixed oxides exhibits enhanced catalytic performance in the removal of formaldehyde. At 70 °C, it can achieve complete formaldehyde removal, with the removal efficiency maintained above 90% for 21 h.[33] BiOBr can achieve a photocatalytic degradation rate of 75% for gaseous benzene under ultraviolet irradiation for 90 min.[34] Researchers have controlled the crystal facets in the preparation of BiOCl, leading to a 94.8% degradation rate of toluene in workshop exhaust within 120 min under static conditions,[35] laying a foundation for studies on the photocatalytic degradation of toluene by BiOX. Despite progress in research on BiOX for VOCs degradation, most existing studies focus on composites of various X (Cl, Br, I) with other photocatalytic materials,[36−40] and further advancements are needed in performance and mechanism studies, particularly in the photocatalytic degradation of toluene gas. There is a paucity of studies comparing BiOX materials for the degradation of toluene. Therefore, this study provides a systematic and comprehensive investigation into the preparation, optimization, characterization, photocatalytic performance, and mechanism of BiOX in the degradation of toluene, which holds significant importance for the removal of indoor VOCs.

In this paper, BiOX (X = Cl, Br, I) nanomaterials were prepared using the straightforward chemical precipitation method, and the prepared BiOX nanomaterials were systematically characterized by various technical means. The photocatalytic performance of BiOX was evaluated in terms of light absorption, material structure, and degradation effect on the pollutant toluene. In addition, we examined the conversion rate of CO_2, a toluene degradation product. Finally, the material with the best degradation effect was selected among BiOX, and the mechanism of its photocatalytic degradation of toluene was deeply analyzed and discussed, and a possible pathway for degrading toluene was given. This study provided an effective strategy for indoor photocatalytic degradation of toluene.

https://doi.org/10.1021/acsomega.4c10658
ACS Omega 2025, 10, 15082−15095

2. MATERIAL AND METHODS

2.1. Experimental Raw Materials. Bismuth nitrate pentahydrate ($Bi(NO_3)_3{\cdot}5H_2O$), potassium chloride, sodium bromide, potassium iodide, ethanol absolute, ethylene glycol, all reagents are Analytical Reagent.

2.2. Preparation of Catalyst. BiOX was prepared as follows: 6 mmol $Bi(NO_3)_3{\cdot}5H_2O$ was weighed and stirred and dispersed into 44 mL of ethylene glycol solvent to obtain a transparent solution A. 6 mmol KCl/NaBr/KI was weighed and stirred and dispersed into 44 mL of deionized water to obtain solution B. Then, solution B was added to solution A to obtain solution C under stirring conditions, and solution C was stirred continuously for 3 h to obtain a homogeneous mixed solution at ambient temperature. Then the mixed solution was filtered and washed with anhydrous ethanol and deionized water for 3 times each and finally dried at 80 °C for 10 h in a blast drying oven to obtain BiOCl/BiOBr/BiOI powders, respectively.

2.3. Characterization Test. The phase structure of the photocatalytic material was characterized and analyzed using an X-ray diffractometer (XRD, Smartlab). The wide-angle scanning range was 2θ = 10°−80°. Scanning electron microscope (SEM, JEM-2010), manufactured by JEOL, Japan, was used to observe the microscopic morphology of the samples and to understand the composition and distribution of the elements in the samples. The Fourier Transform infrared spectrometer (FTIR, Bruker NVENIO-S), produced by Bruker Spectroscopic Instruments, Germany, was tested in the wavelength range of 400−4000 cm^{-1} to gain an in-depth understanding of the structural composition of materials. X-ray photoelectron spectrometer (XPS, Thermo Scientific ESCALAB 250Xi) was used to study the chemical composition of substances and the valence states of component elements, using Al kα rays (hν = 1486.6 eV) as the excitation source. C 1s (284.4 eV) binding energy was used as the energy standard for charge correction. The specific surface area, pore volume, pore size, and distribution of the sample were measured by an N_2-physical desorption apparatus (BET, ASAP 2460) produced by Mack Company. UV−vis DRS test using Agilent-Cary4000 to understand the light absorption properties and range of photocatalytic materials. The electrochemical properties of the materials were tested using the electrochemical workstation CHI600E (silver/silver chloride as the reference electrode) of Shanghai Chenhua Company. The EPR of the material was tested by Bruker EMX PLUS from German. The xenon lamp used in photocatalytic degradation is a 50W Radiant Output (Watts) (CEL-HXF300-T3) from China Education Au-Light as a light source to simulate sunlight. Toluene gas concentration was monitored by Zhejiang Fuli Gas chromatograph (GC9790 Plus).

2.4. Experimental Equipment. A dynamic photocatalytic toluene degradation reaction device was used to simulate the degradation process of toluene gas in the room, in this paper, as shown in Figure 1. The reactor was a self-made double-layer cylinder with a diameter of 9 cm and a height of 13 cm. The reactor cylinder was made of plexiglass and the top cover was made of quartz glass. The cylinder and the top cover were sealed by flanges. Adjusting the height of the xenon lamp so that it was fixed 15 cm directly above the reactor and the lamp was directed vertically toward the center of the bottom of the reactor. A hole was opened on the reactor wall to extend the temperature and humidity sensor into the reactor through the hole and then the hole was sealed to prevent air leakage. The temperature and humidity sensor could monitor the temperature and humidity inside the reactor in real-time. Connecting the reactor outlet to the gas chromatograph. Before the experiment starts, the air tightness check and treatment should be strictly carried out to ensure that the reaction operates under good air-tightness conditions. Then the toluene gas switch was turned on and the toluene concentration was tested every 10 min. When the toluene concentration in the reactor reached equilibrium, the light source was turned on to start the photocatalytic reaction.

2.5. Photocatalytic Activity Test. In this study, the photocatalytic performance of the prepared samples was assessed by determining their efficiency in removing a specified concentration of toluene gas within a dynamic reactor. The efficiency of BiOX in removing toluene gas in a dynamic reactor under xenon lamp irradiation, which simulates sunlight, was determined in order to evaluate the photocatalytic activity. One hundred milligrams of the prepared catalyst were added to five milliliters of ethanol for ultrasonic dispersion, ensuring an even coating on a small Petri dish. The dish was then dried in a 60 °C blower drying oven to facilitate the catalyst's solid adherence to the dish. The catalyst-coated dish was subsequently placed at the bottom of the homemade reactor. To regulate the concentration of toluene pollutants within the reactor, a controlled injection of air and toluene gas was employed to maintain a toluene concentration of approximately 20 ppm. In this study, the temperature within the reactor was maintained at 40 ± 1 °C and the humidity at 30 ± 1% using a gas collection bottle filled with water. After the concentration of toluene had stabilized, a light source utilizing xenon lamps with a total output power of 50 W was turned on to simulate sunlight. Recording the concentration of the gas sample every 10 min. The toluene concentration was detected by the flame ionization detector (FID) in the gas chromatography (GC9790 Plus) connected to the reactor outlet. The gas chromatograph operated with 99.999% nitrogen (N_2) as the carrier gas and the detector temperature was 200 °C. The degradation rate (η) of toluene was calculated by eq 1:

$$\eta = (C_0 - C)/C_0 \times 100\% \quad (1)$$

In the above equation, C_0 represents the equilibrium concentration of toluene before the light is turned on, while C denotes the concentration of toluene in the reactor measured after the light is turned on.

The cyclic stability of the photocatalytic material was tested as follows: after the first test of the material according to the previous procedure, we turned off the xenon lamp and the toluene gas and left the catalyst at the bottom of the reactor without moving it. 12 h later, we turned on the xenon lamp and the toluene gas and started the second experiment, the operation was same in the third, fourth, and fifth experiments. The concentration of CO_2, a degradation product of toluene, was detected using a Flame Ionization Detector (FID) in the gas chromatograph (GC9790). The gas chromatograph was operated with 99.999% nitrogen (N_2) as the carrier gas and a detector temperature of 250 °C. The CO_2 conversion rate was obtained by calculating the ratio of the generated CO_2 concentration to the theoretical CO_2 concentration mineralized by toluene.

https://doi.org/10.1021/acsomega.4c10658
ACS Omega 2025, 10, 15082−15095

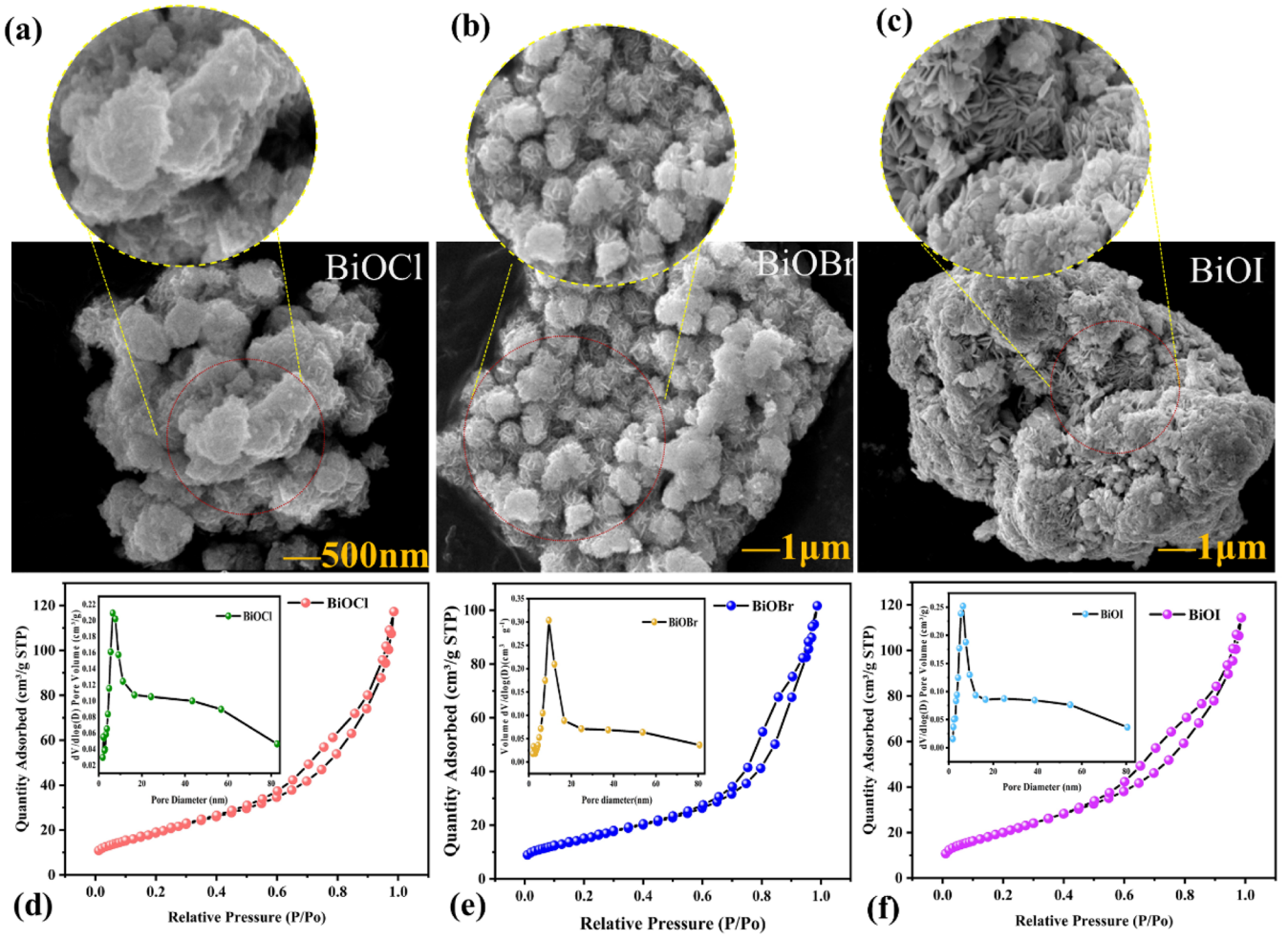

Figure 2. Analysis of the morphological features (a−c), absorption and desorption curves of BiOX materials (d−f).

3. RESULTS AND DISCUSSION

3.1. Analysis of Morphology, Specific Surface Area and Pore Structure. In order to elucidate the morphological characteristics of the BiOX samples, we performed scanning electron microscopy (SEM) analysis. The results are shown in Figure 2a−c. The BiOX samples have small particle sizes and all of them are nanomaterials. Among them, BiOCl presents an irregular lamellar structure formed by the stacking of nanoflakes (Figure 2a), BiOBr presents a circular petal-like structure formed by the agglomeration of nanofine strips (Figure 2b), and BiOI belongs to the agglomerate structure formed by the agglomeration of nanoflakes interspersed and interspersed (Figure 2c). From the figure, it can be seen that BiOBr and BiOI agglomerated to form structures with larger sizes, while the agglomeration of BiOCl was not serious, suggesting that it can provide more active sites, which is favorable for photocatalytic degradation of VOCs.

The pore structure is crucial for photocatalytic materials degradation of VOCs, as it increases the specific surface area and provides a greater number of active sites, thereby improving the adsorption capacity for VOCs. Consequently, we have conducted an analysis of the specific surface area and pore structure. As illustrated in Figure 2d−f, the N_2 adsorption−desorption curves indicate that the adsorption−desorption isotherms of BiOX fall within the H3-type hysteresis loop isotherm, which corresponds to the Langmuir adsorption isotherm Type IV isotherm. This suggests that the materials have a mesoporous structure (2−50 nm), which is confirmed by their pore size distribution curves. The H3-type hysteresis loops may be caused by the formation of slit-like pores due to the aggregation of plate-like particles, which is consistent with the morphology of the materials.[41] The results of specific surface area, pore volume and pore size of BiOX in Table 1 show that BiOI nanoparticles have the largest surface area and the highest surface energy, which indicates that they are in an energetically unstable state and can easily undergo aggregation to reach a stable state, and thus agglomeration occurs, which is consistent with the results shown in Figure 2c. The specific surface area of BiOCl is larger among the three, which is conducive to the adsorption of more reactants and also indicates that it has more active sites on its surface, which can accelerate the generation and transfer of intermediates and products and improve the photocatalytic efficiency.[42] Moreover, the pores act as conduits that facilitate the diffusion of

Table 1. Specific Surface Area, Pore Volume and Pore Size of BiOX

Sample	BiOCl	BiOBr	BiOI
BET Surface Area (m^2/g)	71.68	55.61	76.40
Pore Volume (cm^3/g)	0.1817	0.1581	0.1749
Pore Size (nm)	9.424	10.70	8.372

https://doi.org/10.1021/acsomega.4c10658
ACS Omega 2025, 10, 15082−15095

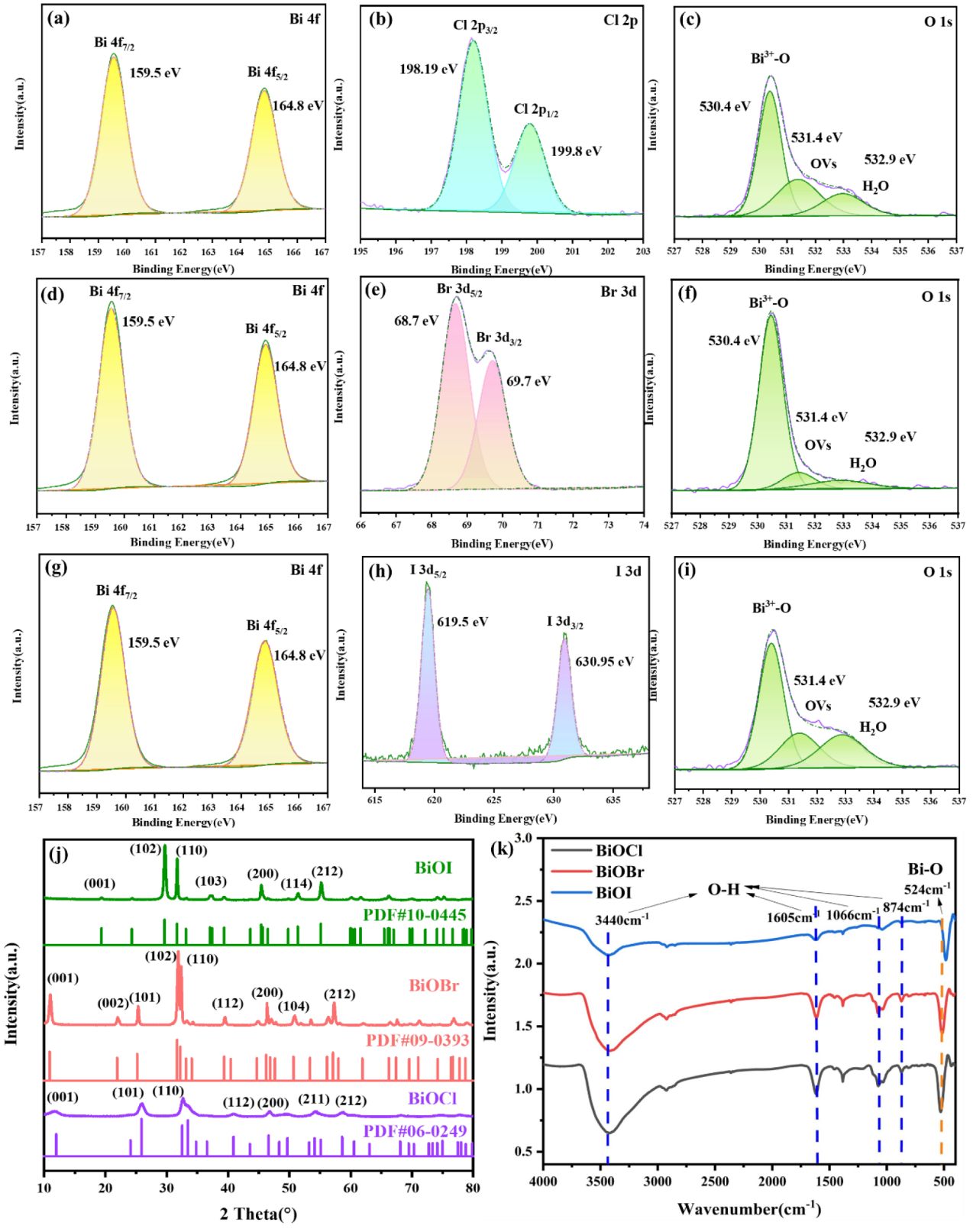

Figure 3. Elemental analysis and surface group composition: (a–i) element analysis by XPS; (j) XRD pattern of BiOX; (k) surface functional group composition by FTIR.

reactants and products, reducing mass transfer resistance and enhancing the efficiency of the photocatalytic process.[43]

3.2. Crystal Structure, Surface Group Composition and Elemental Analysis. The high-resolution XPS spectra of Bi, O, and BiOX were shown in Figure 3. In Figure 3b, the peaks at 198.19 and 199.8 eV are associated with Cl^- 2p3/2 and Cl^- 2p1/2, respectively, indicating the presence of chloride ions (Cl^-).[44] Figure 3e shows the Br 3d peak is divided into

https://doi.org/10.1021/acsomega.4c10658
ACS Omega 2025, 10, 15082−15095

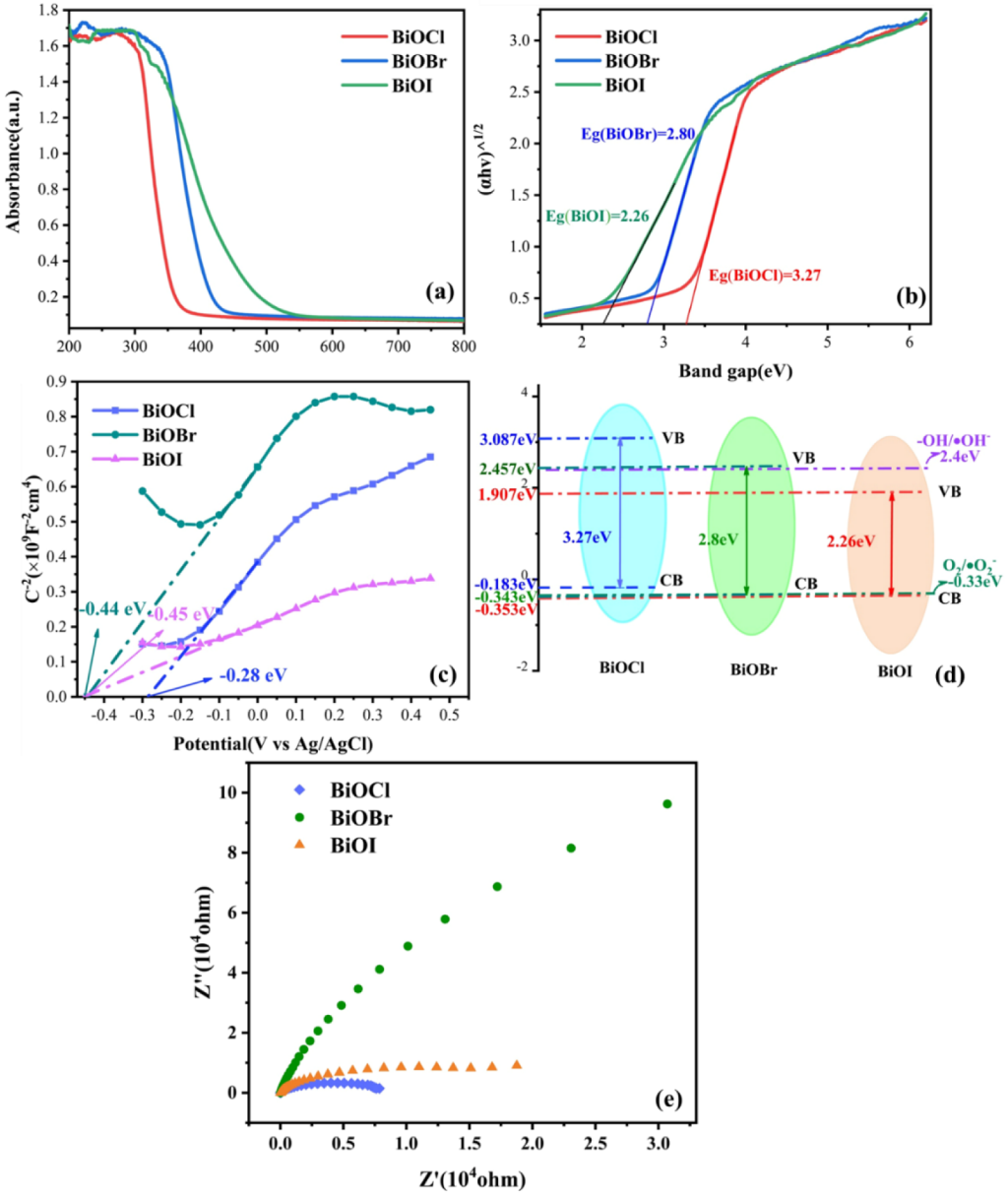

Figure 4. BiOX optical absorption and study of energy band structure: (a) UV−vis DRS spectra of BiOX; (b) $(\alpha h\nu)^{1/2}$ vs optical energy; (c) Mott−Schottky curve; (d) energy band spectrum of BiOX; (e) the electrochemical impedance spectroscopy of BiOX.

three peaks at 68.7 and 69.7 eV, which correspond to bromide ions (Br^-). In Figure 3h, the peaks at 619.5 and 630.95 eV are attributed to the I^- 3d5/2 and I^- 3d3/2, respectively, indicating the presence of iodide ions (I^-).[45] The Bi 4f spectra in Figure 3a,d,g show a pair of peaks at 159.5 and 164.8 eV, indicating the presence of Bi^{3+}. The peaks at 530.4, 531.4, and 532.9 eV in Figure 3c, f, i respectively, are associated with Bi^{3+}−O, oxygen vacancies (OV), and H_2O, indicating the presence of oxygen vacancies in the prepared BiOX. From the figure we can find the oxygen vacancy (OV) peak of BiOCl is obviously the highest and has the largest peak area among the three samples, which proves that it has the most oxygen vacancy (OV) content. The existence of oxygen vacancies is closely related to the photocatalytic performance of materials.[46]

Based on the XRD patterns shown in Figure 3j, it is evident that the synthesized BiOX compounds are in line with the standard card. The distinctive diffraction peaks of BiOCl are detected at 11.72°, 25.93°, 33.05°, 40.87°, 46.71°, 54.31°and 58.66°, which correspond to the (001), (101), (110), (112), (200), (211) and (112) crystal planes, respectively. These peaks indicate that the tetragonal phases of BiOCl are consistent with the standard (JCPDS No. 06−0249) crystal planes. The (001) peak at 11.72° is due to the periodic stacking structure between the [Cl−Bi−O−Bi−O−Cl] layers along the *c*-axis, while the peak at 33.05° belongs to the (110) peak plane, perpendicular to the (001) plane. The (110) peak is the most prominent in the main crystal plane, while the (001) peak is comparatively weaker. This indicates that the product crystals grow along the direction of the (110) crystal plane.[47,48] The peaks of the prepared BiOBr samples are located at 10.95°, 22°, 25.35°, 32°, 32.35°, 39.45°, 46.34°, 50.8° and 57.27°, which correspond to the (001), (002), (101), (102), (110), (112), (200), (104) and (212) crystalline planes. At the same time, it corresponds to the crystal plane of the standard (JCPDS No. 09-0393) for the tetragonal phase

https://doi.org/10.1021/acsomega.4c10658
ACS Omega 2025, 10, 15082−15095

BiOBr. The (102) diffraction peak is the strongest in BiOBr, which is the main crystal plane.[31] On the other hand, the characteristic diffraction peaks of BiOI are located at 19.95°, 29.65°, 31.69°, 37.06°, 45.44°, 51.43° and 55.2°. These peaks correspond to the (001), (102), (110), (103), (200), (114) and (212) crystal planes, respectively. They represent the standard crystal plane of the tetragonal phase BiOI (JCPDS No. 10−0445). The main crystal plane of BiOI is also (102) crystal plane.[49] From the figure, it can be seen that the diffraction peaks of the prepared BiOX samples are all sharp. And there is no obvious impurity peak, which indicates that the prepared BiOI and BiOBr samples have high crystallinity,[50] while BiOCl demonstrates average crystallinity. The high crystallinity of the photocatalyst also reflects that it has abundant catalytic activity centers, which can not only assist light absorption, but also increase the concentration of light-induced electrons, thus affecting the photocatalytic process. It can also affect the migration rate of electrons to the photocatalyst surface, which in turn has an effect on the photocatalytic reaction efficiency.[51,52] Moreover, according to the XRD data, the lattice parameters of BiOCl, BiOBr, and BiOI are calculated to be 3.8887 Å, 3.9107 Å, and 3.9929 Å, respectively. This reveals that as the halogen atoms (Cl, Br, I) increase, the lattice constants also increase in a sequential manner. Although the values are close, they are not identical, indicating that BiOX materials possess similar crystal structures, but the differences in halogen atoms lead to slight variations in atomic bonding within the crystal, resulting in some differences in properties. Furthermore, we determined the crystallite sizes and corresponding full-width at half-maximum (fwhm) for the BiOX materials, with detailed data provided in Table S1. Evidently, as shown in Table S1, the crystallite size of BiOCl can be identified within the synthesized BiOX. This factor is crucial to photocatalytic efficacy. The smaller the crystallite size of these nanomaterials, the more pronounced their photocatalytic activity becomes.[53] This phenomenon is consistent with the superior performance of BiOCl in the degradation of toluene, as concluded in the study.

The FTIR pattern in Figure 3k shows a sharp characteristic absorption peak at 524 cm^{-1}, which is mainly attributed to the symmetric vibration of the Bi−O group in BiOCl. Moreover, O group at 874, 1066, 1605, and 3440 cm^{-1} also produced characteristic peaks, of which the characteristic peaks at 3440 cm^{-1} and 1605 cm^{-1} are mainly created by the telescopic and bending vibrations of adsorbed water surface hydroxyl groups (−OH), suggesting that ethylene glycol can be induced to produce surface hydroxyl groups during the synthesis of the samples.[35,54] In photocatalytic reactions, the hydroxyl groups present on the surface of photocatalysts can act as reactive sites, thereby enhancing the photocatalytic performance of the materials.

3.3. Optical Characterization and Band Structure Analysis. UV−visible diffuse reflectance spectroscopy is a widely utilized technique for evaluating the optical properties of various materials. As seen in Figure 4a, the BiOX samples exhibit strong light absorption characteristics in the UV region. Among them, BiOCl absorbs ultraviolet light. while BiOBr and BiOI can partially respond to visible light. The BiOCl and BiOBr samples have absorption edges around 370 and 430 nm, respectively, while the absorption edge of BiOI is the largest at around 500 nm. The Kubelka−Munk model can be used to transform the UV−vis DRS data, resulting in a plot of $(\alpha h\nu)^{1/2}$ versus optical energy for the samples, as illustrated in Figure 4b Drawing a tangent line from the tilt to the zero axis can provide the energy gap of the samples.[55] The Kubelka−Munk model calculates that the energy gaps of BiOCl, BiOBr, and BiOI are 3.27, 2.80, and 2.26 eV, respectively. Equation 2 is as follows:

$$\alpha h\nu = A(h\nu - E_g)^{n/2} \quad (2)$$

In the eq 2, α, h, ν, A, and E_g represent the optical absorption coefficient, planck constant, optical frequency, constant, and band gap, respectively.[56]

To get the potential of BiOX we measured the Mott−Schottky curves and the data are presented in Figure 4c From the Mott−Schottky curve we can determine that the flat-band potential (E_{FB}) of BiOX is −0.28 eV (vs Ag/AgCl) for BiOCl, −0.44 eV (vs Ag/AgCl) for BiOBr, and −0.45 eV (vs Ag/AgCl) for BiOI. Therefore, when converted to a standard hydrogen electrode, the flat-band potential for BiOCl is −0.083 eV (vs standard hydrogen electrode NHE), −0.243 V (vs standard hydrogen electrode NHE) for BiOBr, and −0.253 eV (vs standard hydrogen electrode NHE) for BiOI. The prepared BiOX are all N-type semiconductors, as indicated by the positive slope of the Mott−Schottky curve. Hence, their E (NHE) is about 0.1 eV higher than the conduction band potential. Therefore, the E_{CB} (BiOCl) is −0.183 eV (vs standard hydrogen electrode NHE), the E_{CB} (BiOBr) is −0.343 V (vs standard hydrogen electrode NHE), and the E_{CB} (BiOI) is −0.353 eV (vs standard hydrogen electrode NHE). According to the Kubelka−Munk model in UV−vis DRS data, the energy gap of BiOX is 3.27 eV for E_g (BiOCl), 2.8 eV for E_g (BiOBr), and 2.26 eV for E_g (BiOI). According to the eq 3:

$$E_{VB} = E_{CB} + E_g \quad (3)$$

E_{VB} (BiOCl) is 3.087 eV (vs standard hydrogen electrode NHE), E_{VB} (BiOBr) is 2.457 V (vs standard hydrogen electrode NHE) and E_{VB} (BiOI) is 1.907 eV (vs standard hydrogen electrode NHE). Based on the acquired data, we have constructed the energy band diagram for BiOX, as depicted in Figure 4d. With reference to this energy band diagram, we are able to delve into the mechanism underlying the photocatalytic degradation of toluene by BiOX.

Electrochemical impedance spectroscopy (EIS) is used to characterize the degree of electron−hole separation. The electrochemical impedance spectroscopy (EIS) spectrum of BiOX in Figure 4e indicates that the Nyquist plot arc radius of BiOCl is significantly smaller than that of BiOBr and BiOI. This indicates that BiOCl exhibits the lowest impedance, implying that the BiOCl photocatalyst possesses the most rapid charge transfer and the highest charge transfer efficiency. As a result, its photocatalytic activity is comparatively superior.[57]

$$N_d = (2/e_0\varepsilon\varepsilon_0)[d(C^{-2})/dV]^{-1} \quad (4)$$

On the other hand, the intrinsic carrier concentration (N_d) can be obtained by using and the eq 4 slope of the Mott−Schottky curve, where e_0 represents the electron charge. ε and ε_0 are the dielectric constant and permittivity of free space of the sample, respectively, and $d(C^{-2})/dV$ is the slope of the linear portion of the Mott−Schottky curve. Thus, the intrinsic carrier concentration (Nd) is inversely proportional to the slope of the linear portion of the Mott−Schottky curve. K(Br) is 1×10^{09}, K(Cl) is 1×10^{09}, and K(I) is 5×10^{08}. The slopes of BiOCl and BiOBr are both lower than the slope of BiOI,

https://doi.org/10.1021/acsomega.4c10658
ACS Omega 2025, 10, 15082−15095

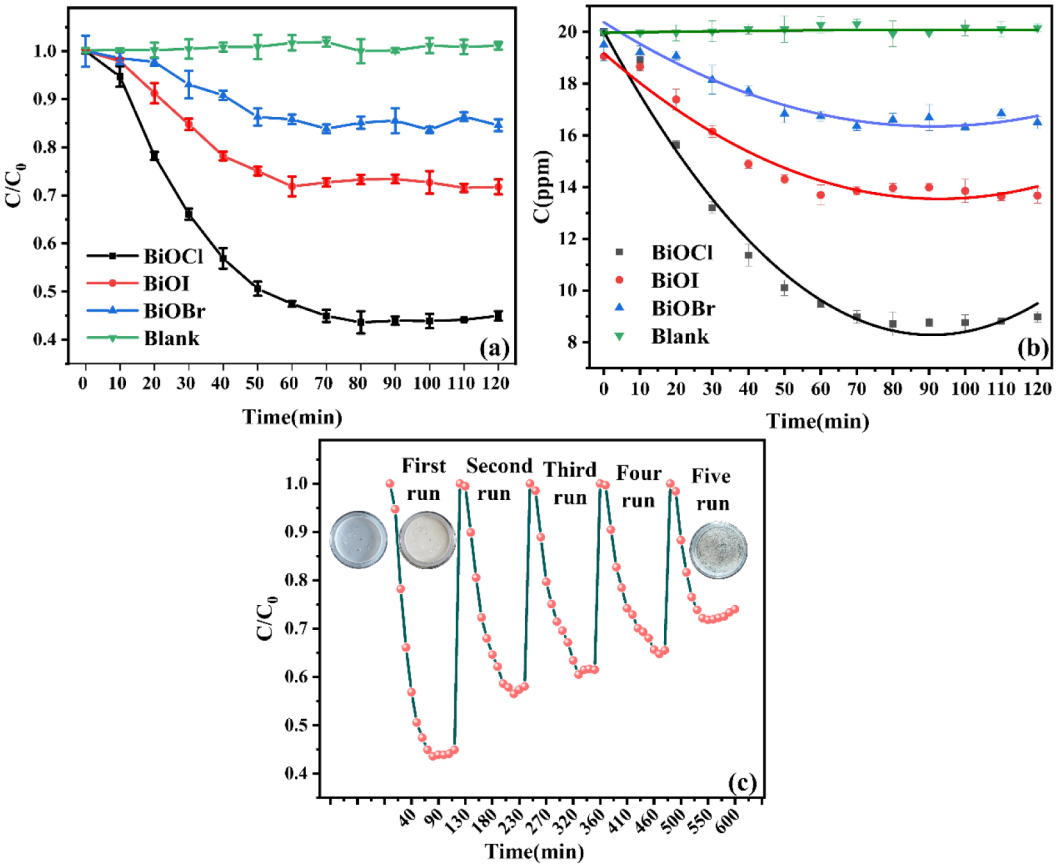

Figure 5. BiOX degradation toluene curves, type of degradation kinetics and reusability of BiOCl: (a) properties of BiOX photocatalytic degradation of toluene; (b) kinetic curves of BiOX degradation of toluene; (c) reproducibility of BiOCl photocatalytic degradation of toluene.

suggesting that both BiOCl and BiOBr have high intrinsic carrier concentration and efficient charge separation.

3.4. Study on Photocatalytic Performance. Before initiating the photocatalytic degradation of toluene, the reactor was enclosed with aluminum foil and subjected to a dark reaction for a minimum duration of 150 min to ensure that the catalyst and the toluene concentration within the reactor achieved adsorption equilibrium. During the reaction, the real-time concentration of toluene in the reactor was monitored by gas chromatography. As shown in Figure 5a, the concentration of toluene in the reactor was basically unchanged within 120 min after xenon lamp irradiation without catalyst. After using BiOX catalyst, the toluene concentrations in the reactor decreased to different degrees within 120 min after light irradiation, with BiOCl having the best degradation rate of 56.41%, BiOBr having the lowest toluene degradation rate of only 16.16%, and BiOI is in the middle of the two at 28.13%.

To further elucidate the degradation process of toluene by BiOX photocatalysis and to assess the photocatalytic performance of BiOX, we constructed the degradation kinetic curves for toluene pollutants within the photocatalytic system. As the kinetic curves of photocatalytic degradation of toluene of the prepared samples in Figure 5b. The curves were obtained using nonlinear least-squares fitting.[58] From the fitted degradation curves in Table 2, it is evident that BiOCl exhibits the steepest slope, indicating that the degradation rate of BiOCl is the most rapid, which is consistent with the experimental results.

To evaluate the recyclability of BiOCl in the photocatalytic degradation of toluene, we repeated the degradation experiments with BiOCl for five times and the comparison results of the degradation rates for five times are shown in Figure 5c. The toluene degradation rate of BiOCl samples gradually decrease after recycling, in which the degradation rate is only 28.17% after the fifth cycle. This result may be due to the recombination of the photogenerated electron−hole pairs after participating in the toluene oxidation reaction, which emits energy and thus partially deactivates them.[59] Subsequently, the compounding of BiOCl photogenerated electron−hole pairs can be further reduced to improve its reusability.

Table 2. Fitted Equations for the Kinetics of Photocatalytic Degradation of Toluene

Sample name	Eitted equation	R^2
BiOCl	$y = 0.00142x^2 - 0.26x + 20.01$	0.9970
BiOBr	$y = 0.000653x^2 - 0.12x + 19.17$	0.9811
BiOI	$y = 0.000486x^2 - 0.09x + 20.37$	0.9548
Blank	$y = -0.0000134x^2 + 0.003x + 19.96$	0.2552

We have compared the findings of this study with those reported in the literature and have included a table in the manuscript to summarize these comparisons. From Table 3, it is evident that existing studies often employ larger quantities of catalysts or combine them with other materials to enhance catalytic activity. Also, it is easier to use the static reaction than the dynamic reaction.[35,60] Therefore, the preferred BiOCl in this study can achieve 56.41% toluene degradation performance in 120 min under natural light with dynamic reaction and a small amount of catalyst, which has a great advantage.

https://doi.org/10.1021/acsomega.4c10658
ACS Omega 2025, 10, 15082−15095

Table 3. Conditions of Photocatalytic Degradation of Toluene by Different Photocatalytic Materials

Sample	Synthesis method	Specific surface area (m^2/g)	Initial concentration	Catalyst dosage (g)	Reactor type	Light source type	Time (min)	Degradation rate (%)	Reference
BiOBr	Solvothermal method	5.3	—	0.5	Static reactor	Ultraviolet/ visible light	300	90/50	61
$BiOBr/Bi_2WO_6$	Hydrothermal process	25.94	—	0.1		Sunlight	120	94.8	36
Bi_2O_3QDs @TiO_2/BiOBr		—	30 ppm	0.2		Visible light	150	94.1	37
$BiOI/Bi_2WO_6$/ACF		788.00	350 mg/m^3	—		Ultraviolet light	240	76.33	38
$BiOCl/Bi_2WO_6$		—	30 ppm	0.2		Sunlight	180	100	39
g-C_3N_4/BiOCl		—					150	85	40
TiO_2		89.50		0.3	Dynamic reactor	Ultraviolet light	120	62	60
F/TiO_2	Chemical precipitation method	10.4	150 ppm	0.03	Static reactor	Sunlight	60	44.7	62
Pd/$SrTiO_3$	Photochemical deposition coupling	58.20	100 ppm	0.15	Dynamic reactor	UV (300−400 nm)	90	80	63
BiOCl	Hydrothermal process/ Solvothermal method	4.48	10 ppm	0.4	Static reactor	Ultraviolet light	120	94.8	35
BiOCl	Chemical precipitation method	71.68	20 ppm	0.1	Dynamic reactor	Sunlight		56.41	This work

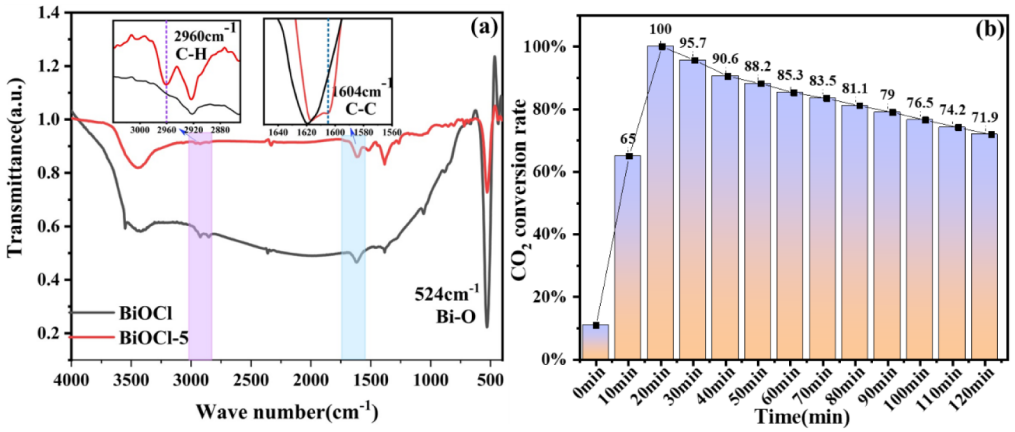

Figure 6. Reaction of BiOCl and toluene and conversion of its product CO_2: (a) comparison of BiOCl before and after degradation of toluene; (b) the conversion rate of CO_2 for toluene degradation by BiOCl.

To gain a deeper understanding of the photocatalytic degradation of toluene by BiOCl, the Fourier-transform infrared (FTIR) spectra of BiOCl samples were analyzed both before and after the degradation process. From the infrared spectra in Figure 6a, it can be seen that the samples show the C−H stretching vibration of toluene occurred in the range of 3000−3100 cm^{-1} after BiOCl had degraded toluene. Moreover, the C−H stretching vibration of toluene methyl is observed at 2960 cm^{-1}, and the toluene C−C benzene ring skeleton vibration is observed at 1604 cm^{-1}. These observations indicate that adsorption and degradation reactions occur during the process of photocatalytic degradation of toluene by BiOCl, leading to a significant reduction in toluene concentration. In addition, the conversion of carbon dioxide, a product of BiOCl degradation of toluene in Figure 6b shows that BiOCl produces free radicals under light to open the benzene ring, ultimately degrading it into carbon dioxide. Furthermore, the conversion rate indicates that there are fewer intermediate products in the degradation process. Although there are physical errors in the experimental operation that caused the CO_2 conversion rate reached to 10% at 0 min, we need to further improve the experimental process to reduce such errors in the subsequent work. However, the overall trend of CO_2 conversion rate is still valid for the experiment. The conversion rate of carbon dioxide can reach up to 100%, thus enabling the complete degradation of toluene pollutants.

We employed electron paramagnetic resonance (EPR) spectroscopy to identify reactive radicals involved in the photocatalytic process, thereby gaining further insight into the mechanism of BiOCl photocatalytic degradation of toluene. DMPO was used as a trapping agent for free radicals ($\bullet O_2^-$ and •OH) in the process. In addition, oxygen vacancies were also determined. The results are shown in Figure 7. The •OH and $\bullet O_2^-$ signals were not captured under dark conditions, and the signal peaks of •OH and $\bullet O_2^-$ were clearly observed after 5 min of natural light irradiation, indicating that BiOCl can produce •OH and $\bullet O_2^-$ under natural light irradiation. Meanwhile quantitatively, the intensity of •OH was slightly higher than that of $\bullet O_2^-$. After 10 min of light irradiation, the intensities of the •OH and $\bullet O_2^-$ signal peaks were slightly weakened. As shown in Figure 7a,b. Figure 7c proves that BiOCl contains more OVs and can play an important role in the photocatalytic reaction process.

https://doi.org/10.1021/acsomega.4c10658
ACS Omega 2025, 10, 15082−15095

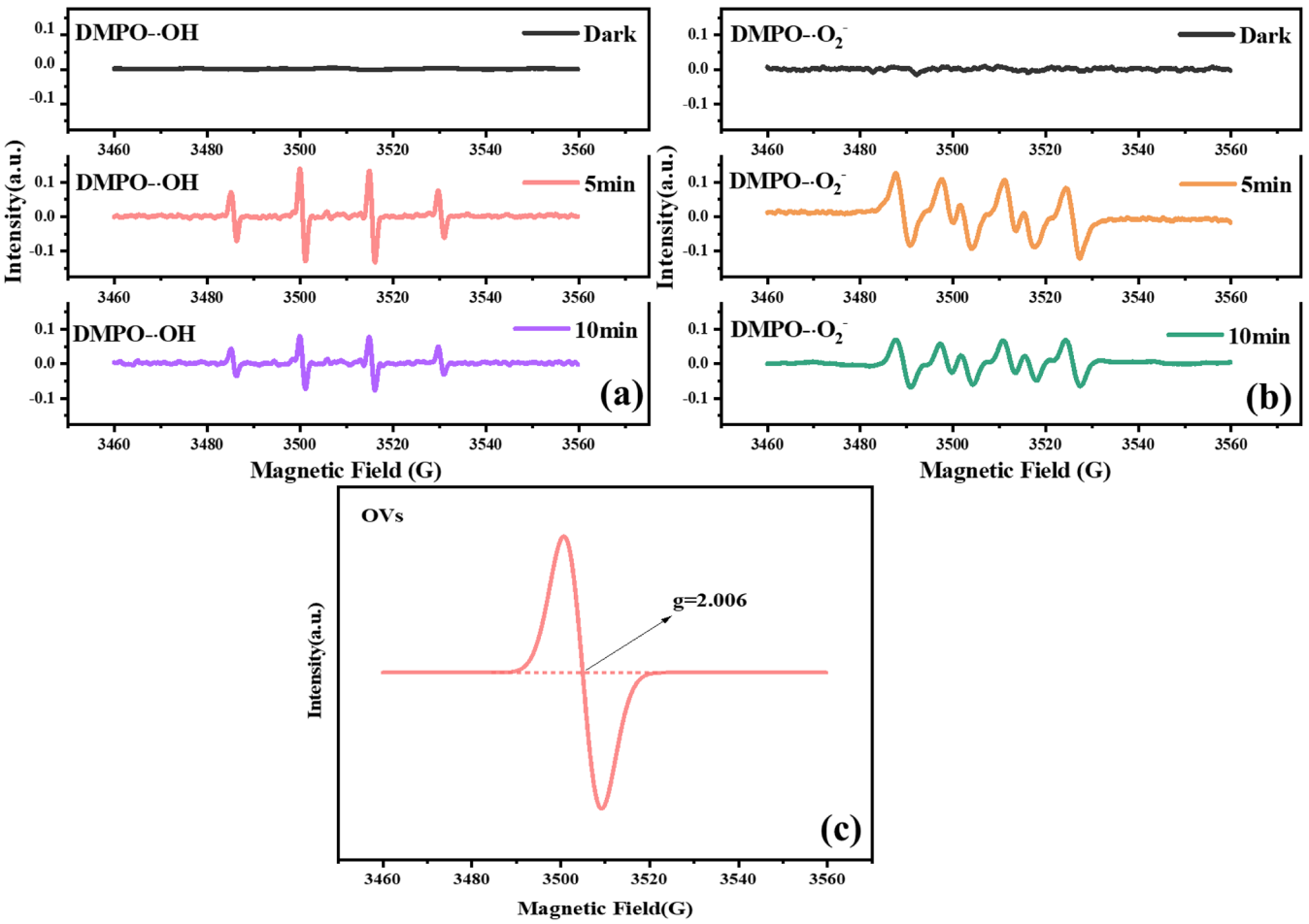

Figure 7. EPR signals on (a) DMPO−•OH, (b) DMPO−$•O_2^-$ and (c) OVs of BiOCl.

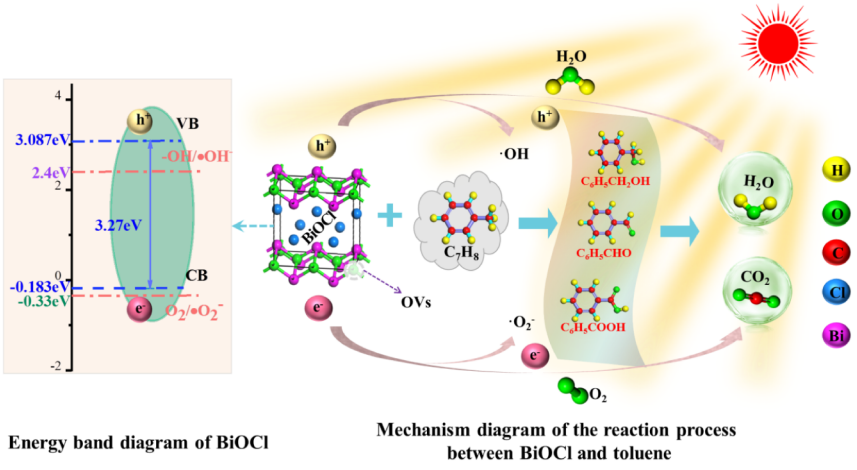

Figure 8. Schematic diagram of the mechanism of gaseous toluene degradation by BiOCl under sunlight.

3.5. Mechanism of Photocatalytic Degradation of Toluene. Through the characterization of the materials and the correlation of their photocatalytic attributes with toluene degradation, it was determined that BiOCl demonstrated the most efficacious degradation of toluene under sunlight. The degradation mechanisms were subjected to analysis and are presented in summary form in Figure 8. BiOCl is excited by light to generate electron−hole pairs, which then move to the surface of BiOCl. The photogenerated holes (h^+) react with OH^- (H_2O) on the catalyst surface to form •OH radicals. These radicals are highly oxidizing and can play a crucial role in the degradation of toluene. Photoelectrons generated during the photocatalytic process react with O_2 on the catalyst surface to produce $•O_2^-$active radicals. From the energy band diagram of BiOCl, its conduction band (CB) potential is −0.183 eV. The redox potential of $O_2/•O_2^-$ (−0.33 eV) is slightly more negative, resulting in less $•O_2^-$ generation. The valence band (VB) potential of BiOCl is 3.087 eV, significantly higher than

https://doi.org/10.1021/acsomega.4c10658
ACS Omega 2025, 10, 15082−15095

the −OH/•OH redox potential (2.4 eV), allowing for the generation of a substantial amount of •OH radicals.[64,65] A large number of •OH radicals and a small number of $•O_2^-$ radicals attack the benzene ring of toluene, breaking its conjugated π-bonds to achieve ring opening and thorough oxidation. The oxidizing photogenerated holes (h^+) can also directly oxidize toluene, effectively degrading it. The XPS test reveals that BiOCl contains specific oxygen vacancies (OVs) that can create defective states below the conduction band minimum, enhancing the absorption capacity of photoelectrons. The presence of oxygen vacancies can serve as unsaturated active sites for coordination, thereby enhancing the adsorption and activation of toluene molecules. This can reduce the activation energy barrier needed for the reaction to take place and accelerate the surface catalytic reaction. Oxygen vacancies can enhance the interaction between BiOCl and toluene π-electrons, facilitating the migration of reactive oxygen species and accelerating the degradation of toluene.[66,67] From the structure of BiOCl, we can observe that the alternation of atoms on the surface of BiOCl results in a low potential barrier. This alternation can facilitate the transfer of charge from the $[BiO_2]^{2+}$ layer to the Cl layer on the surface. This distinctive charge substitution promotes the enhancement of charge separation and conversion, thereby activating pollutants and fostering the generation of reactive oxygen species. Consequently, this process can exert a salutary influence on the degradation of toluene.

The degradation process of toluene can be delineated into several stages: under sunlight, free radicals and holes initiate an attack on the methyl group in toluene. This can culminate in the oxidation of toluene, sequentially yielding benzyl alcohol, benzaldehyde, and benzoic acid, or alternatively, directly resulting in the formation of benzene. These compounds then open the ring to become a variety of alcohols, aldehydes, ketones, olefins, and other short-chain compounds.[17] As the reaction barrier decreases, the free radicals, holes, and oxygen vacancies continue to attack the toluene until it is fully decomposed into carbon dioxide and water, resulting in the complete degradation of the toluene pollutants. This study provides fundamental research and theoretical support for the degradation of indoor VOCs.

4. CONCLUSIONS

BiOX (X = Cl, Br, I) nanophotocatalytic materials were successfully prepared using a simple chemical precipitation method. These materials were effective in degrading toluene gas pollutants in the presence of sunlight. Among the three materials, the degradation effect of BiOCl was the best about 56.41% within 120 min and produced fewer intermediates. The mechanism by which BiOCl degrades toluene gas under natural light is primarily as follows: first, upon illumination, electron−hole pairs are generated. The photogenerated holes (h^+) react with OH^- (from H_2O) to form •OH radicals. The photogenerated electrons react with O_2 to produce $•O_2^-$ radicals. The active radicals •OH and $•O_2^-$ interact with the toluene, disrupting the benzene ring π bonds, while the holes (h^+) may also directly react with the toluene. Additionally, the presence of oxygen vacancies further enhances the adsorption and activation of toluene, reducing the reaction activation energy barrier, accelerating the reaction rate, and strengthening the interaction with the π electrons of toluene. This process enhances the migration of active oxygen species and facilitates the deep degradation of toluene into a series of short-chain compounds, including alcohols, aldehydes, ketones, and alkenes. These compounds are ultimately oxidized to carbon dioxide and water, thereby achieving complete degradation of toluene gas pollutants. Currently, BiOX photocatalytic materials face several challenges in the degradation of VOCs. For instance, the visible light absorption capacity and the efficiency of photogenerated charge carrier separation in BiOX materials require enhancement. Furthermore, the cyclic stability of BiOX materials during photocatalytic degradation is suboptimal. To enhance the photocatalytic degradation of VOCs using BiOX materials, future research directions could focus on modifying the material structure. This includes surface functionalization and composite enhancement to improve visible light utilization and charge carrier separation efficiency. By reducing the recombination of electron−hole pairs, these modifications can further enhance the cyclic stability and photocatalytic activity of BiOX materials in VOCs degradation.

■ ASSOCIATED CONTENT

Data Availability Statement

No data was used for the research described in the article.

Supporting Information

The Supporting Information is available free of charge at https://pubs.acs.org/doi/10.1021/acsomega.4c10658.

Table S1: the crystallite sizes and full-width at half-maximum of synthesized BiOX (PDF)

■ AUTHOR INFORMATION

Corresponding Author

Huiping Song − *Institute of Resources and Environmental Engineering; Shanxi Laboratory for Yellow River; Engineering Research Center of Resource Efficiency Enhancing and Carbon Emission Reduction in Yellow River Basin, Ministry of Education of People's Republic of China, Shanxi University, Taiyuan 030006, China;* orcid.org/0000-0001-8083-1960; Email: songhp@sxu.edu.cn

Authors

Zhenlian Fan − *Institute of Resources and Environmental Engineering; Shanxi Laboratory for Yellow River; Engineering Research Center of Resource Efficiency Enhancing and Carbon Emission Reduction in Yellow River Basin, Ministry of Education of People's Republic of China, Shanxi University, Taiyuan 030006, China*

Shirui Zhang − *Institute of Resources and Environmental Engineering; Shanxi Laboratory for Yellow River; Engineering Research Center of Resource Efficiency Enhancing and Carbon Emission Reduction in Yellow River Basin, Ministry of Education of People's Republic of China, Shanxi University, Taiyuan 030006, China*

Shuyan Cheng − *Institute of Resources and Environmental Engineering; Shanxi Laboratory for Yellow River; Engineering Research Center of Resource Efficiency Enhancing and Carbon Emission Reduction in Yellow River Basin, Ministry of Education of People's Republic of China, Shanxi University, Taiyuan 030006, China*

Zhengjun Feng − *Institute of Resources and Environmental Engineering; Shanxi Laboratory for Yellow River; Engineering Research Center of Resource Efficiency Enhancing and Carbon Emission Reduction in Yellow River*

Basin, Ministry of Education of People's Republic of China, Shanxi University, Taiyuan 030006, China

Hongzhou Lv − *Institute of Resources and Environmental Engineering; Shanxi Laboratory for Yellow River; Engineering Research Center of Resource Efficiency Enhancing and Carbon Emission Reduction in Yellow River Basin, Ministry of Education of People's Republic of China, Shanxi University, Taiyuan 030006, China*

Complete contact information is available at: https://pubs.acs.org/10.1021/acsomega.4c10658

Author Contributions

H.S.: conceptualization, methodology, investigation, resources, supervision, review and editing, funding acquisition. Z.F.: conceptualization, methodology, investigation, resources, data curation, writing- original draft preparation. Z.S.: conceptualization, methodology. S.C.: conceptualization, methodology, resources. Z.F.: conceptualization, methodology, investigation, resources. H.L.: Conceptualization, methodology, resources. All authors have read and agreed to the published version of the manuscript.

Notes

The authors declare no competing financial interest.

■ ACKNOWLEDGMENTS

This work was finically supported by Central Guidance Fund for Local Science and Technology Development Projects (YDZJSX2024D003) and Fund Program for the Scientific Activities of Selected Returned Overseas Professionals in Shanxi Province (20230005).

■ REFERENCES

(1) Passi, A.; Nagendra, S. M; Maiya, M. P. Characteristics of indoor air quality in underground metro stations: A critical review. *Build. Environ.* **2021**, *198*, 107907.

(2) Wen, L. X.; Fu, H. X.; Hu, J. C.; Huang, S. Y. Analytical solution of coupled heat-moisture-VOCs transfer process in liquid desiccant dehumidifier for indoor VOCs removal. *Build. Environ.* **2023**, *227*, 109791.

(3) Yu, L. L.; Wang, Y. Y.; Zou, J.; Jiang, J. Z. Recent Advance of Photo/Electrocatalytic Degradation of Formaldehyde in Indoor Air. *J. Liaocheng Univ.* **2023**, *36* (5), 56−68.

(4) Saqlain, S. B.; Cha, J.; Kim, S. Y.; Sung, J. Y.; Choi, M. C.; Seo, H. O.; Kim, Y. D. Impact of humidity on the removal of volatile organic compounds over Fe loaded TiO_2 under visible light irradiation: Insight into photocatalysis mechanism by operando DRIFTS. *Mater. Today Commun.* **2021**, *26*, 102119.

(5) Zhou, C.; Zhan, Y.; Chen, S.; Xia, M.; Ronda, C.; Sun, M.; Chen, H. Y.; Shen, X. Y. Combined effects of temperature and humidity on indoor VOCs pollution: Intercity comparison. *Build. Environ.* **2017**, *121*, 26−34.

(6) Li, H.; Song, Z.; Mao, Y.; Zhang, X.; Huang, Z.; Liu, W.; Gao, H.; Dong, D. Degradation mechanism of toluene over Ce-M(Cu, Co and Fe) catalysts: Effect of oxygen vacancies on reaction intermediates. *Appl. Surf. Sci.* **2024**, *652*, 159272.

(7) Gennaro, G. D.; Gennaro, L. D.; Mazzone, A.; Porcelli, F.; Tutino, M. Indoor air quality in hair salons: Screening of volatile organic compounds and indicators based on health risk assessment. *Atmos. Environ.* **2014**, *83*, 119−126.

(8) Yan, M.; Zhai, Y.; Shi, P.; Yang, H.; Zhao, H. Emission of volatile organic compounds from new furniture products and its impact on human health. *Hum. Ecol. Risk. Asess.* **2018**, *25* (7), 1886−1906.

(9) Wallace, L. A. Human exposure to volatile organic pollutants: implications for indoor air studies. *Annu. Rev. Env. Resour.* **2001**, *26*, 269−301.

(10) Kim, K. J.; Kim, H. J.; Khalekuzzaman, M.; Yoo, E. H.; Jung, H. H.; Jang, H. S. Removal ratio of gaseous toluene and xylene transported from air to root zone via the stem by indoor plants. *Environ. Sci. Pollut. R* **2016**, *23* (7), 6149−6158.

(11) Mikheeva, N. N.; Zaikovskii, V. I.; Larichev, Y. V.; Mamontov, G. V. Toluene abatement on Ag-CeO_2/SBA-15 catalysts: synergistic effect of silver and ceria. *Mater. Today Chem.* **2021**, *21*, 100530.

(12) Li, X.; Cui, R.; Yang, B. J.; Xie, S. Y.; Zeng, G. M.; Zheng, H. W.; Zheng, H. L. Research progress on indoor VOC pollution and control. *Mini-Rev. Org. Chem.* **2023**, *20* (2), 124−135.

(13) Wu, Z. M.; Meng, X. J.; Zhao, Z. X. Efficient removal of VOCs enabled by triboelectric-photocatalytic coupling effect. *Nano Energy* **2024**, *132*, 110364.

(14) Benltifa, M.; Brahmi, C.; Dumur, F.; Limousy, L.; Bousselmi, L.; Lalevée, J. A comparison study of the photocatalytic efficiency of different developed photocatalysts/polymer composites. *Eur. Polym. J.* **2022**, *181*, 111660.

(15) Zhong, L.; Haghighat, F. Photocatalytic air cleaners and materials technologies−abilities and limitations. *Build. Environ.* **2015**, *91*, 191−203.

(16) Chen, S.; Wang, Q.; Shi, M.; Ye, H.; Wu, Z. Deep oxidation of NO by a hybrid system of plasma-N-type semiconductors: high-energy electron-activated pseudo photocatalysis behavior. *Environ. Sci. Technol.* **2018**, *52*, 8568−8577.

(17) Li, J.; Dong, X.; Zhang, G.; Cui, W.; Cen, W.; Wu, Z.; Lee, S.; Dong, F. Probing ring-opening pathways for efficient photocatalytic toluene decomposition. *J. Mater. Chem. A* **2019**, *7*, 3366−3374.

(18) Zhang, X.; Chen, J.; Jiang, S.; Zhang, X.; Bi, F.; Yang, Y.; Wang, Y. X.; Wang, Z. Enhanced photocatalytic degradation of gaseous toluene and liquidus tetracycline by anatase/rutile titanium dioxide with heterophase junction derived from materials of institut lavoisier-125(Ti): degradation pathway and mechanism studies. *J. Colloid Interface Sci.* **2021**, *588*, 122−137.

(19) Wang, H.; Liao, B.; Lu, T.; Ai, Y.; Liu, G. Enhanced visible-light photocatalytic degradation of tetracycline by a novel hollow BiOCl@CeO_2 heterostructured microspheres: Structural characterization and reaction mechanism. *J. Hazard. Mater.* **2020**, *385*, 121552.

(20) Sun, Y.; Younis, A.; Kim, K.; Kumar, V. Potential utility of BiOX photocatalysts and their design/modification strategies for the optimum reduction of CO_2. *Sci. Total Environ.* **2023**, *863*, 160923.

(21) Gao, Y.; Zhu, S.; Wang, Z.; Chen, G.; Wang, C. Visible-driven photocatalytic activity and stability of Bi_2O_3 enhanced by CQDs. *J. Mater. Sci.* **2024**, *59*, 19492−19507.

(22) Khedr, T. M.; Wang, K.; Kowalski, D.; El-Sheikh, S. M.; Abdeldayem, H. M.; Ohtani, B.; Kowalska, E. Bi_2WO_6-based Z-scheme photocatalysts: Principles, mechanisms and photocatalytic applications. *J. Environ. Chem. Eng.* **2022**, *10* (3), 107838.

(23) Kamble, G. S.; Natarajan, T. S.; Patil, S. S.; Thomas, M.; Chougale, R. K.; Sanadi, P. D.; Siddharth, U. S.; Ling, Y. C. $BiVO_4$ as a sustainable and emerging photocatalyst: synthesis methodologies, engineering properties, and its volatile organic compounds degradation efficiency. *Nanomaterials* **2023**, *13* (9), 1528.

(24) Ni, Z.; Sun, Y.; Zhang, Y.; Dong, F. Fabrication, modification and application of $(BiO)_2CO_3$-based photocatalysts: a review. *Appl. Surf. Sci.* **2016**, *365*, 314−335.

(25) Ahmad, I.; Shukrullah, S.; Naz, M. Y.; Ullah, S.; Assiri, M. A. Designing and modification of bismuth oxyhalides BiOX (X = Cl, Br and I) photocatalysts for improved photocatalytic performance. *J. Ind. Eng. Chem.* **2022**, *105*, 1−33.

(26) Shi, M.; Li, G. N.; Li, J. M. X.; Tao, X.; Zeng, B.; Pidko, E. A.; Li, R. G.; Li, C. Intrinsic facet-dependent reactivity of well-defined BiOBr nanosheets on photocatalytic water splitting. *Angew. Chem. Int. Ed.* **2020**, *59*, 6590−6595.

(27) Li, X.; Hu, Y.; Dong, F.; Huang, J.; Han, L.; Deng, F.; Luo, Y.; Xie, Y.; He, C.; Feng, Z.; Chen, Z. Non-noble-metallic Ni_2P nanoparticles modified OV-BiOBr with boosting photoelectrochemical hydrogen evolution without sacrificial agent. *Appl. Catal., B* **2023**, *325*, 122341.

(28) Guan, C.; Hou, T.; Nie, W.; Zhang, Y.; Duan, Q.; Zhao, X. Sn^{4+} doping enhanced inner electric field for photocatalytic performance promotion of BiOCl based nanoflowers. *Appl. Surf. Sci.* **2022**, *604*, 154498.
(29) Yuan, Z.; Jiang, Z. Applications of BiOX in the photocatalytic reactions. *Molecules* **2023**, *28* (11), 4400.
(30) Nava-Núñez, M. Y.; Jimenez-Relinque, E.; Cruz, A. M. L.; Castellote, M. Photocatalytic NOx Removal in Bismuth-Oxyhalide (BiOX, X = I, Cl) Cement-Based Materials Exposed to Outdoor Conditions. *Catalysts* **2022**, *12* (9), 982.
(31) Ren, X. J.; Gao, M. C.; Zhang, Y. F.; Zhang, Z. Z.; Cao, X. Z.; Wang, B. Y.; Wang, X. X. Photocatalytic reduction of CO_2 on BiOX: Effect of halogen element type and surface oxygen vacancy mediated mechanism. *Appl. Catal., B* **2020**, *274*, 119063.
(32) Lu, P.; Zhang, N.; Wang, Y.; Wang, Y. D.; Zhang, J. L.; Cai, Q. Y.; Zhang, Y. H. Synthesis of BiOX-Red Mud/Granulated Blast Furnace Slag Geopolymer Microspheres for Photocatalytic Degradation of Formaldehyde. *Materials* **2024**, *17* (7), 1585.
(33) Wang, X. L.; Wu, G. D.; Ma, Y. W. Low-Temperature Oxidation Removal of Formaldehyde Catalyzed by Mn-Containing Mixed-Oxide-Supported Bismuth Oxychloride in Air. *Catalysts* **2022**, *12* (3), 262.
(34) Liu, Y.; Yin, Y. Q.; Jia, X. Q.; Cui, X. Y.; Tian, C. R.; Sang, Y. H.; Liu, H. Synthesis process and photocatalytic properties of BiOBr nanosheets for gaseous benzene. *Environ. Sci. Pollut. Res.* **2016**, *23*, 17525−17531.
(35) Rao, J. X.; Chen, X. T.; Zheng, X. Z.; Du, C. M. Study on the regulation of BiOCl and its mechanism of photocatalytic degradation of toluene. *Atmos. Pollut. Res.* **2023**, *14* (10), 101854.
(36) Da, K.; Mao, X. Q.; Ma, Y. Q.; Wu, L.; Li, Y.; Zou, S. J.; Cao, S. B.; Yang, J.; Fan, X. M. Fabricating BiOBr/Bi_2WO_6 S-scheme heterojunction with interface modification strategy for efficient photocatalytic degradation of gaseous toluene. *Mater. Today Commun.* **2024**, *40*, 109612.
(37) Xu, H.; Yang, J.; Li, Y.; Fu, F.; Da, K.; Cao, S. B.; Chen, W. T.; Fan, X. M. Fabrication of Bi_2O_3 QDs decorated TiO_2/BiOBr dual Z-scheme photocatalysts for efficient degradation of gaseous toluene under visible-light. *J. Alloys Compd.* **2023**, *950*, 169959.
(38) Wang, Y. Q.; Jiang, S.; Liu, F.; Zhao, C. C.; Zhao, D. F.; Li, X. F. Study on preparation and toluene removal of BiOI/Bi_2WO_6/ACF photocatalyst. *Appl. Surf. Sci.* **2019**, *488*, 161−169.
(39) Yang, J.; Yang, L.; Fang, M.; Li, L.; Fu, F.; Xu, H.; Li, M. G.; Fan, X. M. A compact Z-scheme heterojunction of BiOCl/Bi_2WO_6 for efficiently photocatalytic degradation of gaseous toluene. *J. Colloid Interface Sci.* **2023**, *631* (partB), 44−54.
(40) Fu, F.; Yang, J.; Xu, H.; Li, Y.; Cao, S. B.; Da, K.; Chen, W. T.; Fan, X. M. Enhancing the photocatalytic performance of the g-C_3N_4/BiOCl heterojunction in gaseous toluene degradation via K^+ decoration in g-C_3N_4. *Chem. Eng. Sci.* **2023**, *276*, 118793.
(41) Meng, X. C.; Zhang, Z. S. Bi_2MoO_6 co-modified by reduced graphene oxide and palladium(Pd^{2+} and Pd^0)with enhanced photocatalytic decomposition of phenol. *Appl. Catal., B* **2017**, *209*, 383−393.
(42) Meng, X. C.; Zhang, Z. S. New insight into BiOX(X = Cl, Br, and I) hierarchical microspheres in photocatalysis. *Mater. Lett.* **2018**, *225*, 152−156.
(43) Wilczewska, P.; Bielicka-Giełdoń, A.; Szczodrowski, K.; Malankowska, A.; Ryl, J.; Tabaka, K.; Siedlecka, E. M. Morphology regulation mechanism and enhancement of photocatalytic performance of BiOX (X = Cl, Br, I) via mannitol-assisted synthesis. *Catalysts* **2021**, *11* (3), 312.
(44) Liu, C.; Zhou, J.; Su, J.; Guo, L. J. Turning the unwanted surface bismuth enrichment to favourable $BiVO_4$/BiOCl Heterojunction for enhanced photoelectrochemical performance. *Appl. Catal., B* **2019**, *241*, 506−513.
(45) Wang, Z. D.; Chu, Z.; Dong, C.; Wang, Z.; Yao, S. Y.; Gao, H.; Liu, Z. Y.; Liu, Y.; Yang, B.; Zhang, H. Ultrathin BiOX(X = Cl, Br, I) nanosheets with exposed {001} facets for photocatalysis. *ACS Appl. Nano Mater.* **2020**, *3* (2), 1981−1991.
(46) Li, H.; Long, B.; Ye, K. H.; Cai, Y. P.; He, X. Y.; Lan, Y. Q.; Yang, Z. J.; Ji, H. B. A recyclable photocatalytic tea-bag-like device model based on ultrathin Bi/C/BiOX(X = Cl, Br) nanosheets. *Appl. Surf. Sci.* **2020**, *515*, 145967−145967.
(47) Jie, L.; Ying, Y.; Zhang, L. Z. Bismuth oxyhalide nanomaterials: layered structures meet photocatalysis. *Nanoscale* **2014**, *6* (15), 8473−8488.
(48) Yu, H. M.; Han, Q. F. Effect of reaction mediums on photocatalytic performance of BiOX (X = Cl, Br, I). *Oot. Mater.* **2021**, *119*, 111399.
(49) Ji, L.; Wang, H.; Yu, R. Heterogeneous photocatalysts BiOX/$NaBiO_3$ (X = Cl, Br, I): Photo-generated charge carriers transfer property and enhanced photocatalytic activity. *Chem. Phys.* **2016**, *478*, 14−22.
(50) Fu, S. M.; Li, G. S.; Wen, X. C.; Fan, M.; Liu, J. X.; Zhang, X. C.; Li, R. Effect of calcination temperature on microstructure and photocatalytic activity of BiOX (X = Cl, Br). *Trans. Nonferrous Met. Soc. China* **2020**, *30*, 765−773.
(51) Wei, Z. D.; Liu, J. Y.; Fang, W. J.; Qin, Z.; Jiang, Z.; Shangguan, W. F. A visible-light driven novel layered perovskite oxyhalide Bi_4MO_8X (M = Nb, Ta; X = Cl, Br) constructed using BiOX(X= Cl, Br) for enhanced photocatalytic hydrogen evolution. *Catal. Sci. Technol.* **2018**, *8* (15), 3774−3784.
(52) Irshad, A.; Shazia, S.; Muhammad, N. Y.; Ullah, S.; Assiri, M. A. Designing and modification of bismuth oxyhalides BiOX(X=Cl, Br and I) photocatalysts for improved photocatalytic performance. *J. Ind. Eng. Chem.* **2022**, *105*, 1−33.
(53) Strauss, M.; Pastorello, M.; Sigoli, F. A.; Silva, J. M. D. S. E.; Mazali, I. O. Singular effect of crystallite size on the charge carrier generation and photocatalytic activity of nano-TiO_2. *Appl. Surf. Sci.* **2014**, *319*, 151−157.
(54) Gao, X.; Zhang, X.; Wang, Y.; Peng, S.; Yue, B.; Fan, C. Rapid synthesis of hierarchical BiOCl microspheres for efficient photocatalytic degradation of carbamazepine under simulated solar irradiation. *Chem. Eng. J.* **2015**, *263*, 419−426.
(55) Welter, E. S.; Garg, S.; Gläser, R.; Goepel, M. Methodological Investigation of the Band Gap Determination of Solid Semiconductors via UV/Vis Spectroscopy. *ChemPhotochem* **2023**, *7* (6), No. e202300001.
(56) Chen, X.; Zhuang, C.; Wang, X.; Liao, A.; Li, L.; Liu, Q.; Tang, Y.; Wu, C.; Shen, Q.; Yu, Z. Two-Step Synthesis of Laminar Vanadate via a facile hydrothermal route and enhancing the photocatalytic reduction of CO_2 into solar fuel through tuning of the oxygen vacancies by in situ vacuum illumination treatment. *ACS Appl. Energy Mater.* **2018**, *1* (12), 6857−6864.
(57) Majhi, D.; Das, K.; Mishra, A.; Dhiman, R.; Mishra, B. G. One pot synthesis of CdS/BiOBr/$Bi_2O_2CO_3$: a novel ternary double Z-scheme heterostructure photocatalyst for efficient degradation of atrazine. *Appl. Catal., B* **2020**, *260*, 118222.
(58) Belghiti, M.; Tanji, K.; Mersly, L. E. L.; Lamsayety, I.; Ouzaouit, K.; Faqir, H.; Benzakour, I.; Rafqah, S.; Outzourhit, A. Fast and non-selective photodegradation of basic yellow 28, malachite green, tetracycline, and sulfamethazine using a nanosized ZnO synthesized from zin core. *React. Kinet., Mech. Catal.* **2022**, *135*, 2265−2278.
(59) Wang, L.; Huang, X.; Han, M.; Lyu, L.; Li, T.; Gao, Y. W.; Zeng, Q. Y.; Hu, C. Efficient inhibition of photogenerated electron-hole recombination through persulfate activation and dual-pathway degradation of micropollutants over iron molybdate. *Appl. Catal., B* **2019**, *257*, 117904.
(60) Zeng, Y.; Zhan, Y.; Xie, R.; Hu, K.; Cao, J.; Lei, D.; Liu, B.; He, M.; Huang, H. Toluene oxidation over mesoporous TiO_2 in a combined process of wet-scrubbing and UV-catalysis. *Chemosphere* **2020**, *244*, 125567.
(61) Feng, Y.; Li, L.; Li, J.; Wang, J.; Liu, L. Synthesis of mesoporous BiOBr 3D microspheres and their photodecomposition for toluene. *J. Hazard. Mater.* **2011**, *192* (2), 538−544.

https://doi.org/10.1021/acsomega.4c10658
ACS Omega 2025, 10, 15082−15095

(62) Yuan, S.; Chen, M.; Qin, X.; Chen, X.; Zhang, J.; Zhang, C. Effects of surface fluoride modification on TiO_2 for the photocatalytic oxidation of toluene. *J. Environ. Sci.* **2025**, *147*, 561−570.
(63) Gao, D.; Wang, B.; Bi, W.; Xue, F.; Cui, M.; Fei, Z.; Li, L.; Qiao, X. Plasma-induced surface interactions of $Pd/SrTiO_3$ catalyst for improved performance of photocatalytic degradation of toluene. *J. Environ. Chem. Eng.* **2024**, *12* (5), 113544.
(64) Wu, Y.; Zhao, X.; Huang, S.; Li, Y.; Zhang, X.; Zeng, G.; Niu, L.; Ling, Y.; Zhang, Y. Facile construction of 2D $g\text{-}C_3N_4$ supported nanoflower-like $NaBiO_3$ with direct Z-scheme heterojunctions and insight into its photocatalytic degradation of tetracycline. *J. Hazard. Mater.* **2021**, *414*, 125547.
(65) Low, J.; Jiang, C.; Cheng, B.; Wageh, S.; Al-Ghamdi, A. A.; Yu, J. A review of direct Z-scheme photocatalysts. *Small Methods* **2017**, *1* (5), 1700080.
(66) Wang, Y.; Zhang, Y.; Zhu, X.; Liu, Y.; Wu, Z. Fluorine-induced oxygen vacancies on TiO_2 nanosheets for photocatalytic indoor VOCs degradation. *Appl. Catal., B* **2022**, *316*, 121610.
(67) Wei, X.; Li, K.; Zhang, X.; Tong, Q.; Ji, J.; Cai, Y.; Gao, B.; Zou, W.; Dong, L. CeO_2 nanosheets with anion-induced oxygen vacancies for promoting photocatalytic toluene mineralization: toluene adsorption and reactive oxygen species. *Appl. Catal., B* **2022**, *317*, 121694.

https://doi.org/10.1021/acsomega.4c10658
ACS Omega 2025, 10, 15082−15095